Ocean Dynamics (2016) 66:589–603
DOI 10.1007/s10236-016-0939-x

Unstructured-mesh modeling of the Congo river-to-sea continuum

Yoann Le Bars[1] · Valentin Vallaeys[1] · Éric Deleersnijder[2,3] · Emmanuel Hanert[4] · Loren Carrere[5] · Claire Channelière[6]

Received: 27 August 2015 / Accepted: 22 February 2016 / Published online: 14 March 2016

Abstract With the second largest outflow in the world and one of the widest hydrological basins, the Congo River is of a major importance both locally and globally. However, relatively few studies have been conducted on its hydrology, as compared to other great rivers such as the Amazon, Nile, Yangtze, or Mississippi. The goal of this study is therefore to help fill this gap and provide the first high-resolution simulation of the Congo river-estuary-coastal sea continuum. To this end, we are using a discontinuous-Galerkin finite element marine model that solves the two-dimensional depth-averaged shallow water equations on an unstructured mesh. To ensure a smooth transition from river to coastal sea, we have considered a model that encompasses both hydrological and coastal ocean processes. An important difficulty in setting up this model was to find data to parameterize and validate it, as it is a rather remote and understudied area. Therefore, an important effort in this study has been to establish a methodology to take advantage of all the data sources available including nautical charts that had to be digitalized. The model surface elevation has then been validated with respect to an altimetric database. Model results suggest the existence of gyres in the vicinity of the river mouth that have never been documented before. The effect of those gyres on the Congo River dynamics has been further investigated by simulating the transport of Lagrangian particles and computing the water age.

Keywords Multi-scale modelling · Congo river-to-sea continuum · Tides · Water age · Satellite altimetry

Responsible Editor: Alexander Barth

This article is part of the Topical Collection on the *47th International Liège Colloquium on Ocean Dynamics, Liège, Belgium, 4-8 May 2015*

Yoann Le Bars and Valentin Vallaeys contributed equally to this manuscript

✉ Emmanuel Hanert
emmanuel.hanert@uclouvain.be

[1] Institute of Mechanics, Materials, and Civil Engineering (IMMC), Université catholique de Louvain, 4 avenue Georges Lemaître, B-1348 Louvain-la-Neuve, Belgium

[2] Institute of Mechanics, Materials, and Civil Engineering (IMMC), Earth and Life Institute (ELI), Université catholique de Louvain, 4 avenue Georges Lemaître, B-1348 Louvain-la-Neuve, Belgium

[3] Delft Institute of Applied Mathematics (DIAM), Delft University of Technology, Mekelweg 4, 2628CD Delft, The Netherlands

[4] Earth and Life Institute (ELI), Université catholique de Louvain, 2 Croix du Sud, B-1348 Louvain-la-Neuve, Belgium

[5] Collecte Localisation Satellites (CLS), 8-10 rue Hermès, Parc technologique du canal, 31520 Ramonville Saint-Agne, France

[6] Total S.A.,EP/DEV/TEC/GEO, Tour Newton, 9, place des Vosges, Quartier Gambetta, La Défense 5, 92400 Courbevoie, France

1 Introduction

The Congo River is among the longest, deepest, and strongest rivers in the world. It has a length of about 4700 km. Its discharge varies between 2.3×10^4 m^3 s^{-1} and 8×10^4 m^3 s^{-1}, with an average of about 4.5×10^4 m^3 s^{-1} (Eisma and van Bennekom 1978). The river bed alternates between very shallow areas of less than 5 m in the branching

area downstream of Boma to depths of more than 400 m at the river mouth (Fig. 1). The Congo River watershed covers an area of 3.7 $\times 10^6$ km^2 (Savoye et al. 2009). Although the river has a relatively low annual sediment discharge (5.5 $\times 10^7$ ty^{-1}) compared to that of the Amazon River, it supplies a large volume of particulate and dissolved organic matter to the ocean, both in the surface plume and at the sea bottom through turbidity in the estuarine canyon.

Yet, despite its importance, the Congo River remains understudied. This is mostly because of its remoteness and the difficulty to conduct field campaigns in that region. Most publications documenting riverbed constituents, river discharge, and currents in the estuary were produced more than 30 years ago (e.g., Meulenbergh 1968; Peters and Sterling 1973; Meulenbergh 1974; Eisma and van Bennekom 1978; Eisma et al. 1978; Eisma and Kalf 1984). Other studies have mostly focused on the dynamics of the river plume over the continental shelf and on the transport of sediments towards the deep ocean (see for instance Hopkins et al. (2013)).

The coastal dynamics is driven by the peculiar topography and bathymetry of the estuary. At the coast, the estuary is partly shut off from the sea by beach barriers located South at Ponta do Padrao and North at Banana (Eisma and van Bennekom 1978). The lower section of the estuary is characterized by the presence of a deep canyon originating downstream of the shallow water area, dropping abruptly to 100 m depth and continuing as a narrow trench down to the floor of the Angola basin to at least 3500 m depth. It therefore connects directly the river with the deep sea. At the present time, such a canyon is unique, but similar ones existed during the Pleistocene in the Mississippi and Niger river mouths (Heezen et al. 1964; Burke 1972). This canyon is a significant challenge when modeling this area, especially when considering baroclinic phenomena.

Remoteness and lack of data explain why so few modeling studies of the Congo River have been published. A notable exception is the recent article of Denamiel et al. (2013), which focuses on the river plume dynamics. Their results reveal that the variations of the Congo River plume and the freshwater transport are controlled by the interdependence of various environmental conditions: the persistent wind forcing and the complex ocean circulation actively impact the far-field dynamics while the unique geomorphology of the Congo estuary drives both the far-field and the near-field plume. We are not aware of any study that has tried to investigate the dynamics of the Congo river-to-sea continuum.

The goal of this paper is therefore to fill in this gap by presenting the first simulations of the Congo river-to-sea continuum, from Matadi down to the coastal sea. By doing so, we want to highlight the key processes driving the hydrodynamics and show how they influence the flow regimes of this system. We hope that such simulations will give rise to a renewed interest in this region and motivate the organization of new field campaigns. To achieve these objectives, we have applied a high-resolution, unstructured-mesh model to this complex multi-scale system. The bulk of the paper is devoted to the model formulation and parameterization (Section 2), and its extensive validation both in the sea and river environments (Section 3). We then move on to analyze the peculiar dynamics of the river estuary by using different diagnoses such as Lagrangian particles and water-age tracers (Section 4). Conclusions and perspectives are presented in Section 5. More technical aspects related the collection and treatment of the various sources of data are detailed in Appendix (Section A).

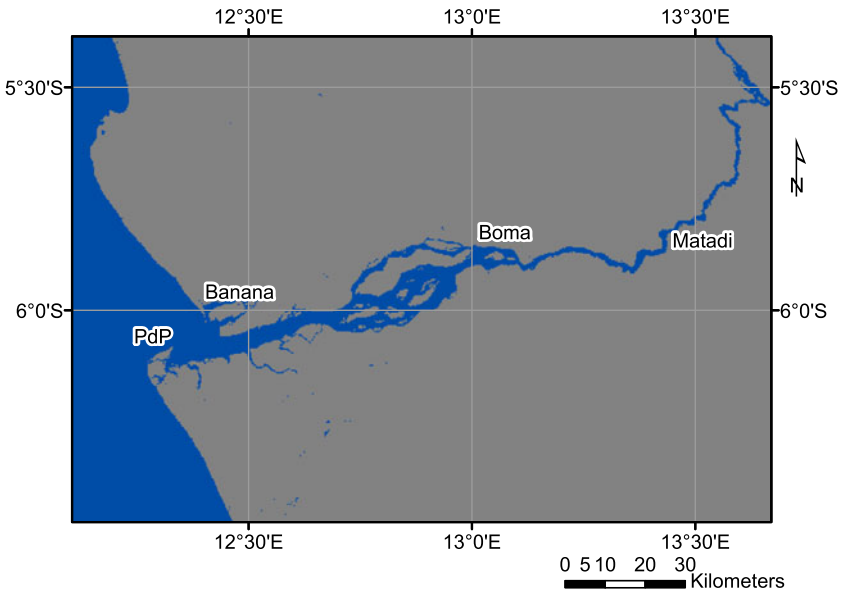

Fig. 1 Overview of the Congo river-to-sea continuum. The average river discharge is about 4.5×10^4 m^3 s^{-1}. Matadi is located about 10 km downstream rapids that prevent navigation. On the map, PdP stands for Ponta do Padrao. Image courtesy of Julien Radoux

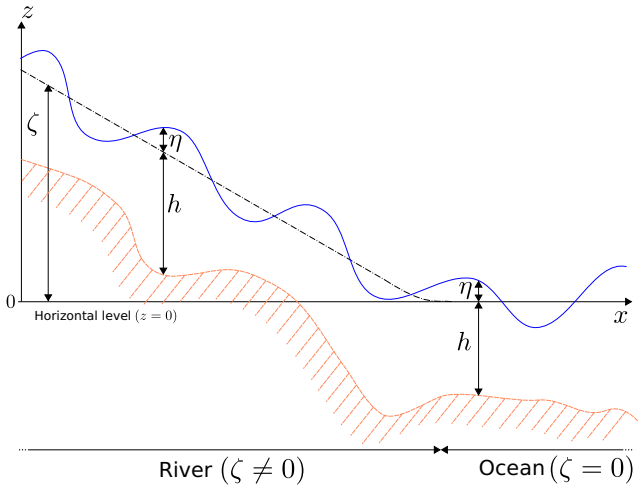

Fig. 2 In the river, the water reference level is above sea level. The variable ζ represents the difference between the reference levels in the river and in the ocean. The latter corresponds to the $z = 0$ horizontal level. The gradient of ζ acts as an extra down-slope forcing term in the river. This gradient is, however, very small since ζ = 8 m at Matadi, located about 150 km from the river mouth

2 Model formulation and parameterization

We used SLIM 2D, the depth-integrated version of the second-generation Louvain-la-neuve Ice-ocean Model[1]. As we focus in this study only on barotropic processes, such a model is sufficient. SLIM 2D solves the the 2D depth-integrated shallow-water equations with multi-rate time stepping schemes. The model equations are discretized on an unstructured mesh by means of the discontinuous Galerkin finite element method. SLIM 2D's multi-scale capabilities make it ideally suited for hydrodynamic processes in complex environments. It has been successfully used in several coastal oceans and estuaries around the world (e.g., Lambrechts et al. 2008b; de Brye et al. 2010, 2011; Thomas et al. 2014).

The model governing equations are:

$$\frac{\partial \eta}{\partial t} + \nabla \cdot (H\overline{\boldsymbol{u}}) = 0, \tag{1}$$

$$\frac{\partial \overline{\boldsymbol{u}}}{\partial t} + (\overline{\boldsymbol{u}} \cdot \nabla)\,\overline{\boldsymbol{u}} + f\boldsymbol{e}_z \times \overline{\boldsymbol{u}} = -g\nabla(\eta + \zeta) + \overline{\boldsymbol{\Psi}}, \tag{2}$$

with η the elevation of the free surface, $H = h + \eta$ the total water height, h is bathymetry, $\overline{\boldsymbol{u}}$ the depth-averaged velocity, f Coriolis' parameter, $\boldsymbol{e}_z$ the vertical unit vector pointing upward, g the gravitational acceleration, and ζ is the height of the reference water level with respect to the horizontal level (see Fig. 2). ∇ is the horizontal del operator, which can be defined in two dimensions as $\nabla = \left(\frac{\partial}{\partial x}, \frac{\partial}{\partial y}\right)^{\mathsf{T}}$, $\cdot$ is the scalar product and $\times$ the cross product. $\overline{\boldsymbol{\Psi}}$ is defined as follows:

$$\overline{\boldsymbol{\Psi}} = \boldsymbol{F} + \boldsymbol{D}, \tag{3}$$

where $\boldsymbol{F}$ represents external forcing, such as the tides generating forces and the wind stress, and $\boldsymbol{D}$ represents dissipative terms, i.e., bottom friction and horizontal momentum diffusion. In this paper, we take:

$$\boldsymbol{D} = -\frac{g\,\|\overline{\boldsymbol{u}}\|\,\overline{\boldsymbol{u}}}{C_h^2 H} + \frac{1}{H}\nabla \cdot (H\nu_h \nabla \overline{\boldsymbol{u}}), \tag{4}$$

with C_h Chézy's coefficient and ν_h the horizontal eddy viscosity. Chézy's coefficient is derived from Manning's coefficient n with the following expression:

$$C_h = \frac{H^{1/6}}{n}. \tag{5}$$

Following Lambrechts et al. (2008b), we take $n = 2.35 \times 10^{-2}$ m$^{-1/3}$ s.

One of the main difficulty to set up a model of the Congo River estuary is to gather enough data to characterize the domain and parameterize or force the model. The remoteness of this region means the datasets are quite scarce. This is particularly the case for the bathymetry and coastlines for which we had to merge different sources of information such as GEBCO 2008 (Monahan 2008), nautical charts, and qualitative information about the location of navigation channels in order to obtain comprehensive datasets that seamlessly encompass the entire computational domain. The construction of these datasets is described in Appendix A and the resulting bathymetry is shown in Fig. 3.

Regarding regional external forcings, we consider the wind and the global circulation in the Atlantic Ocean. Following Smith and Banke (1975), the wind stress $\boldsymbol{F}_{ws}$ is parameterized as follows:

$$\boldsymbol{F}_{ws} = 10^{-3}\left(0.630\,\|\boldsymbol{v}_w\| + 0.066\,\|\boldsymbol{v}_w\|^2\right)\boldsymbol{v}_w, \tag{6}$$

with $\boldsymbol{v}_w$ the wind velocity 10 m over the sea surface (in m s^{-1}). Wind fields were retrieved from the European Centre for Medium-range Weather Forecasts (ECMWF). The global circulation is imposed using a Flow Relaxation Scheme method (FRS) inspired by the work of Martinsen and Engedahl (1987). It implies the use of a relaxation term whose goal is to keep the model velocity close enough to the depth averaged velocity of a global circulation model. In this study, we used HYCOM (Chassignet et al. 2007), which provides 3D currents on a $^1/_{12}°$ grid. The global circulation forcing $\boldsymbol{F}_{gc}$ is:

$$\boldsymbol{F}_{gc} = \gamma\,(\overline{\boldsymbol{u}}_\star - \overline{\boldsymbol{u}}), \tag{7}$$

with $\overline{\boldsymbol{u}}_\star$ the depth average velocity obtained from the global circulation model and $\gamma = {}^1/_\tau$ the inverse of the relaxation time.

[1] http://www.climate.be/slim/

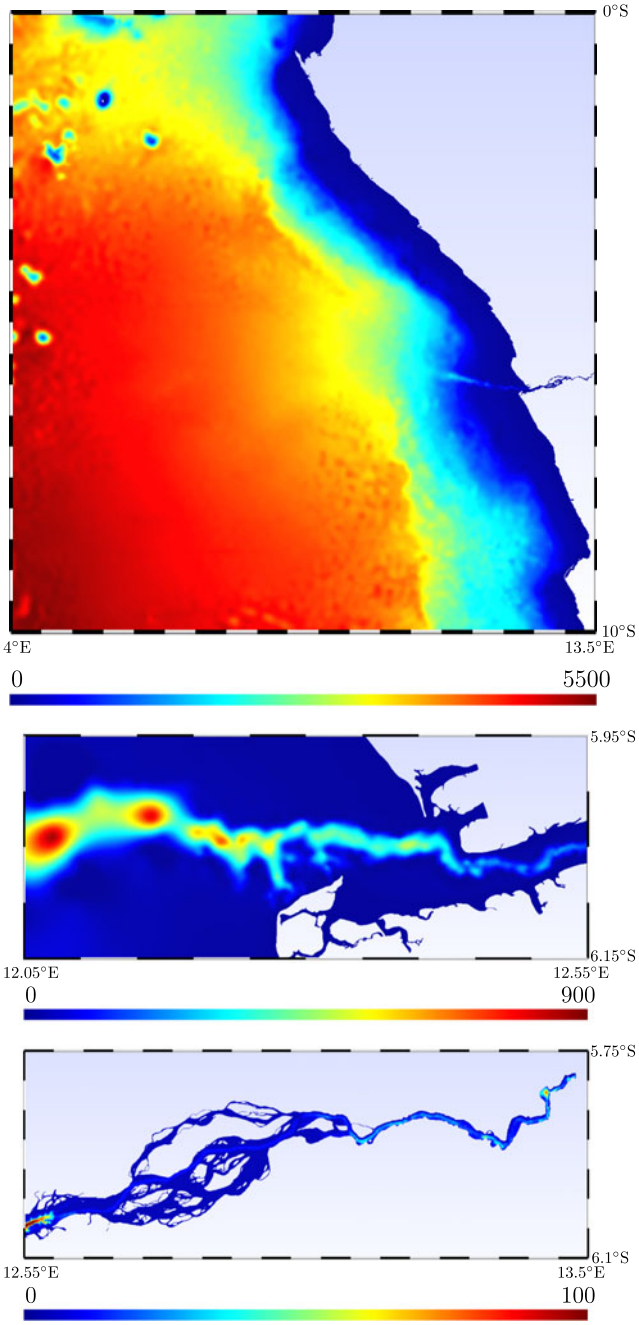

Fig. 3 Bathymetry over the entire computational domaine (*top panel*, in m) and close-up views on the Congo River estuary (*middle panel*) and further upstream in the river (*bottom panel*). The water depth ranges from 5 m in the shallowest parts of the river to about 5.7 km in the deep ocean. The submarine canyon that extends well onto the continental shelf and connects the river with the deep ocean is clearly seen in the middle panel

In the deep ocean, τ is defined such that the relaxation time is longer than the dominant tidal wave—in the study area, this dominant tidal component is M_2 and we have set $\gamma = 10^{-6}\ \mathrm{s}^{-1}$—while it is set to zero in the river estuary to prevent the global circulation from interfering with the river dynamics. A smooth transition between values of γ in the deep ocean and its values in the river is ensured by a linear interpolation over several kilometers. This is obviously a rather crude and simple method to couple our barotropic model with a baroclinic one. As with most coupling procedures, it can lead to spurious oscillations in the region where the FRS is applied. In this work, we have not considered different coupling strategies and investigated which one was the most suitable. Instead, we have considered a quite large computational domain so that the FRS is only weakly applied in the region of interest. The complete external forcing term can then be expressed as follows:

$$\boldsymbol{F} = 10^{-3}\left(0.630\,\|\boldsymbol{v}_w\| + 0.066\,\|\boldsymbol{v}_w\|\right)\boldsymbol{v}_w + \gamma\left(\overline{\boldsymbol{u}}_\star - \overline{\boldsymbol{u}}\right). \tag{8}$$

In Eq. 2, the term $-g\nabla\zeta$ can be seen as an extra forcing term that causes the water to flow down the river slope. For the sake of simplicity, we have considered the same coordinate system in the river and in the ocean. As a result, the river flow is not strictly aligned with the horizontal axis. In the case of the Congo River, such an approximation is nonetheless valid as the difference of altitude between the river inflow at Matadi and the river mouth is only 8 m. The average river slope is thus of only 0.005 %. For a steeper river, a more accurate approach would be to use a curvilinear coordinate system always parallel to the river surface. In that case, the z-axis is not vertical and the weight of the fluid has thus components in the momentum equation governing the evolution of u and v. The approach adopted here is similar to the river slope forcing terms used in many hydrological models (see for instance Jansen 1979; Graf and Altinakar 1993, 1996; Hervouet and Van Haren 1996).

Regarding boundary conditions, we use three formulations. On the open ocean boundary, elevation and current due to oceanic tides are imposed as a Flather condition (Flather 1976). In this study, we have used FES2012 global tidal solution (e.g., Lyard et al. 2006; Carrère et al. 2012), which provides 32 tidal constituents on a 1/16° grid. On river open boundary, the river discharge is imposed using daily flow rate measurements collected at Inga, about 30 km upstream of Matadi. A free-slip condition is finally imposed on land boundaries. It should be noted that the Flather boundary conditions are not integrated within the FRS scheme used to impose the global circulation. Since we use a discontinuous Galerking framework to derive the discrete equations, we have to compute fluxes through all the edges of the mesh. On the open boundaries, these fluxes are computed by using the Flather boundary condition. The FRS is only imposed "inside" each element of the mesh through the forcing term $\mathbf{F}_{gc}$ in the momentum equation. This term does not appear in the boundary fluxes. There is therefore no direct interaction between Flather and FRS as the former

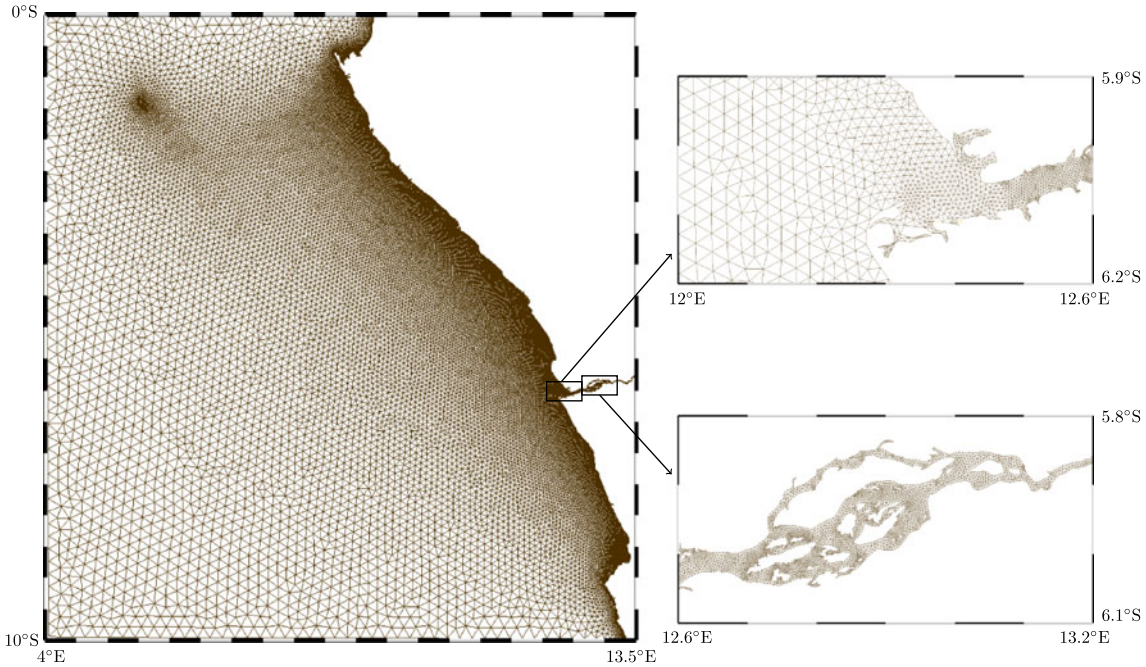

Fig. 4 The model unstructured mesh contains about 25,000 nodes and 51,000 elements. The smallest edge is about 200 m long inside the river, while the longest is about 20 km long in the deep ocean. The mesh covers an area of about 1000 km × 1000 km

is imposed only on boundary edges and the other only inside mesh elements.

The model unstructured mesh has been produced by means of GMSH[2] (Geuzaine and Remacle 2009; Lambrechts et al. 2008a) by using the bathymetry and coastline databases we reconstructed. It contains about 25,000 nodes and 51,000 elements. Its smallest edge is about 200 m in length inside the river, while its largest is about 20 km long in the deep ocean. As suggested by Fig. 4, there are two major advantages in using unstructured meshes. The first is that such meshes can smoothly fit the complex geometry of coastlines and river banks. Using structured meshes would require complex downscaling methods, involving several nested grids. The second is the ability to choose where to have the finest resolution. In the deep ocean, dominant phenomena have large scales, so we can use large elements, while in the river and estuary, dominant phenomena are characterized by smaller length scales that require a higher resolution.

Because of non-linear tides, we have placed deep ocean boundaries quite far away from the river estuary. Indeed, such tides develop on shelves (such as Congo River shelf), and they are usually difficult to prescribe on the open boundaries. Moreover, non-linear tides are generally not referenced in global databases, except for M_4. As a consequence, we have chosen to set the limits of the computational domain in the deep ocean, where boundary conditions are easier to define. In those regions, we assume that tides not present in the tidal atlas we use (see Section 2) are negligible and are locally generated inside the modelling area.

[2] http://geuz.org/gmsh/

3 Model validation

As mentioned before, data that can be used to validate the model are difficult to collect, as they need to span a large understudied area over a long period of time. In this study, we have used a global tidal analysis based on Topex/Poseidon and Jason 1 and 2 altimetric datasets to validate the modeled elevation. According to Eisma and van Bennekom (1978), the tides in the Congo River estuary are semi-diurnal and of a comparatively small range: at Banana, the maximum range is 1.90 m (at spring tide) and the minimum range is 0.30 m (at neap tide), for an average of 0.80 m.

To perform a complete tidal analysis, we have run a 13-month simulation, from January 1st, 2011 until January 31st, 2012. Figure 5 shows the modeled M_2 tidal component. As expected, the amplitude is amplified by the shelf break and near the river mouth, and damped in the shallow water areas. These features are consistent with previous observations (e.g., Meulenbergh 1974). The M_2 amplitude is 0.4 m in the deep ocean, 0.6 m at the river mouth, and negligible at Matadi. Its propagation is mainly from south to north.

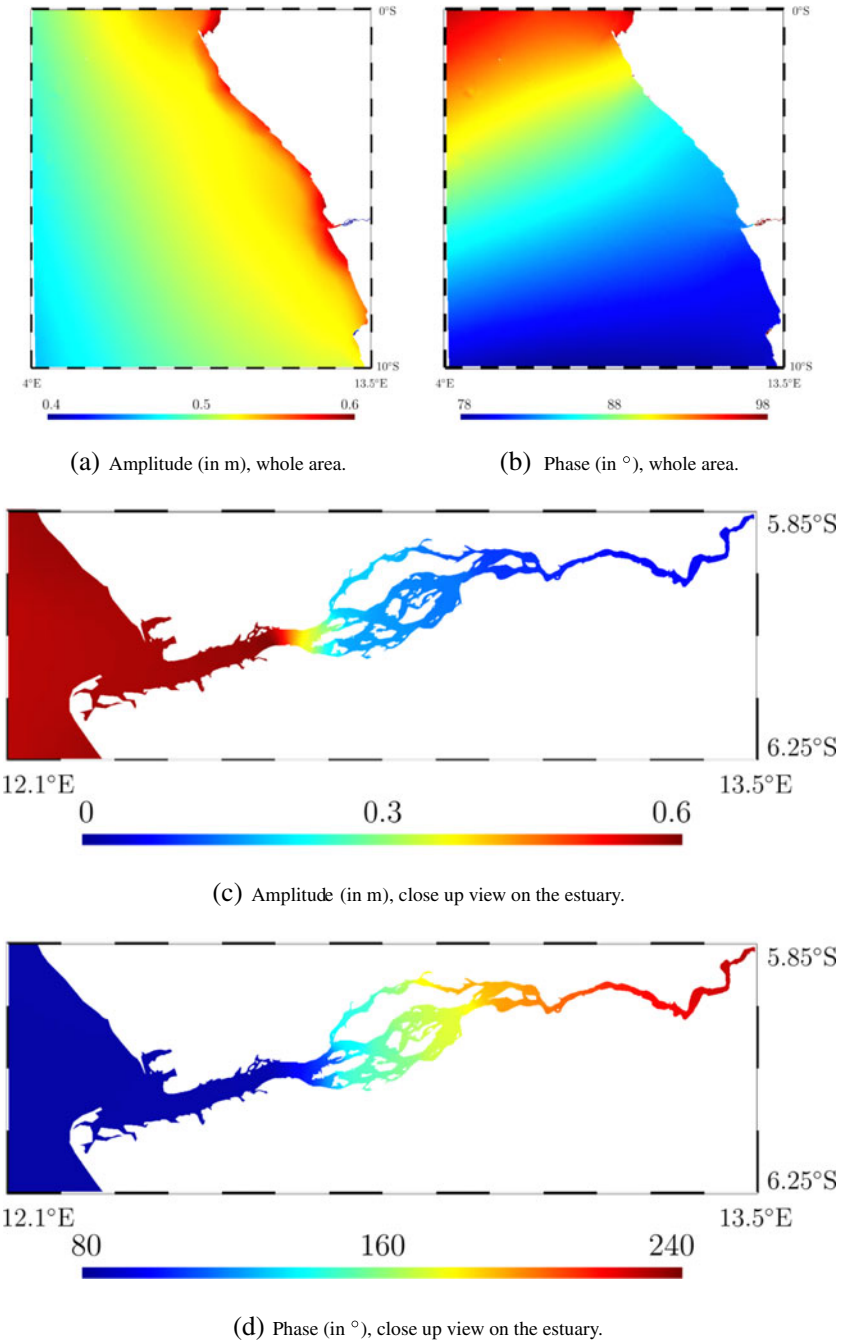

(a) Amplitude (in m), whole area.

(b) Phase (in °), whole area.

(c) Amplitude (in m), close up view on the estuary.

(d) Phase (in °), close up view on the estuary.

Fig. 5 M_2 tidal component in the Congo River mouth and neighboring ocean. While crossing shelf break, the tide is amplified, reaching 0.6 m of amplitude in the river mouth. In shallow waters area, the tidal amplitude is attenuated. M_2 propagates from south to north

We then made a comparison between model results and altimetric tidal data. Figure 6 shows the altimetry tracks along which we have surface elevation observations, as well as the difference with model results. Table 1 sums up global statistics for this comparison. In this table, components are given in order of decreasing amplitude. While M_2, S_2, and N_2 amplitudes are of the order of tens of centimetres, K_1 amplitude is of several centimetres, when Q_1 and M_4 amplitudes are of few millimetres. For these two last components, we are reaching the precision of altimeters, therefore the validation should be considered with caution. We did not investigate additional tidal components, as their amplitudes are too small to yield a significant value.

As shown in Fig. 6 and Table 1, differences between the simulated and observed M_2 tidal amplitude are small (2.5 % on average). As expected, the absolute error in amplitude is more important in areas where the tidal amplitude is the largest, i.e., near the coast where the tidal wave has been amplified after shelf break. The RMS error is relatively small as well (4 %). Validation of other tidal component also shows a good accuracy as, if we exclude Q_1 and M_4, the most important relative mean error on amplitude is 5.2 % for

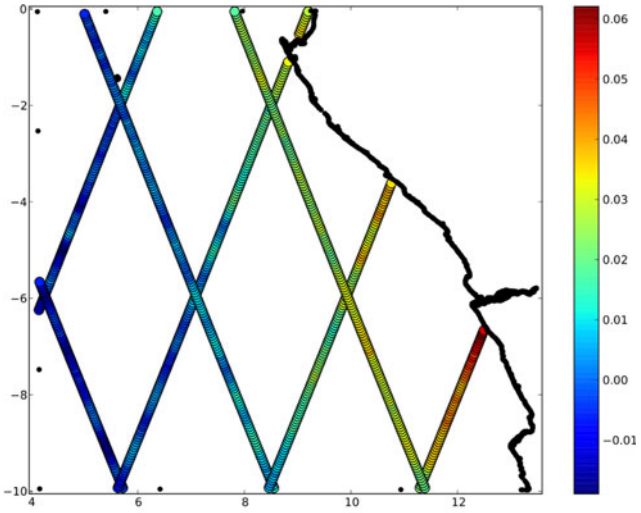

(a) Absolute error on amplitude with regard to altimetry (in m).

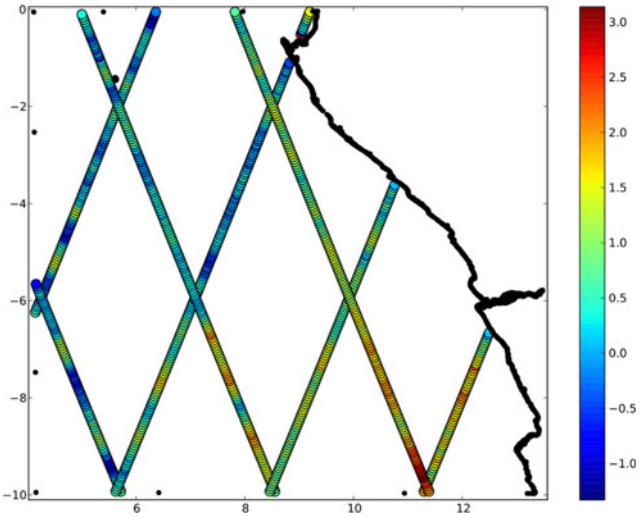

(b) Absolute error on phase with regard to altimetry (in °).

Fig. 6 Comparison between the simulated and observed M_2 tidal component. Observations are based on altimetric data from Topex/Poseidon and Jason 1 and 2

S_2, the maximum relative RMS on amplitudes is 15.4 % for O_1. The maximum absolute error on phase occurs also for O_1, with a mean error of 2.9° and a RMS of 27.86°, which are still satisfactory.

Whatever the component, our model suggests a significant attenuation of the amplitude and a phase shift when entering the uncharted zone downstream of Boma. This is not surprising since the river is quite shallow and has a rugged topography in that area. Hence, dissipation is expected to be important. However, since we lack tidal observations in this region, we cannot exclude that some other phenomena may be at work.

Table 1 Modeled tidal components validation by comparison with the altimetric database from Topex/Poseidon and Jason 1 and 2

Tidal	Errors on amplitude				Errors on phase	
	Absolute (cm)		Relative (%)		Absolute (°)	
Component	Mean	RMS	Mean	RMS	Mean	RMS
M_2	1.26	2.09	2.53	4.09	0.17	0.72
S_2	0.86	1.10	5.23	6.73	–1.67	1.98
N_2	0.19	0.31	1.86	3.12	1.05	1.66
K_1	–0.12	1.01	–0.02	11.33	–2.64	4.29
K_2	0.28	0.39	6.03	8.43	–0.21	2.05
P_1	–0.02	0.42	1.41	14.92	1.00	6.86
O_1	–0.05	0.20	–2.18	15.40	2.95	27.86
Q_1	–0.06	0.18	–2.83	55.38	–2.47	15.60
M_4	–0.08	0.19	–10.49	52.05	19.44	29.13

The previous validation has been further refined by using measurements from a tidal gauge located at Pointe-Noire (4.8° S, 11.9° E), about 160 km North of the river estuary. Measurements from this tidal gauge run from 1 April 2011 to 29 June 2014. We made a comparison between our model and measurements from this tidal gauge. This comparison is summed up in Table 2. The results are consistent with the comparison against altimetric data, as, once again without considering Q_1 nor M_4, the most important relative error on amplitude is -13.5 % for K_1, and the most important absolute error on phase is $-16°$ for O_1.

Validating the model specifically in the river environment is more challenging as there are very few observations in this remote region. In the absence of field data, we have used again satellite data. We considered a Jason-2 satellite track that crosses the Congo River near the island of Mateba, about 30 km downstream of Boma and about 50 km from the river mouth. In this region, the tidal signal is still present

Table 2 Modeled tidal components validation with regard to the tidal gauge located at Pointe-Noire

Tidal	Errors on amplitude		Errors on phase
Component	Absolute (cm)	Relative (%)	Absolute (°)
M_2	0.79	1.54	–6.54
S_2	0.92	5.43	–11.60
N_2	0.08	0.82	–5.89
K_1	–1.28	–13.46	–2.95
K_2	0.38	8.24	–9.00
P_1	–0.28	–9.94	0.79
O_1	–0.14	–10.77	–15.98
Q_1	–0.14	–21.68	–3.26
M_4	–0.07	–15.58	22.87

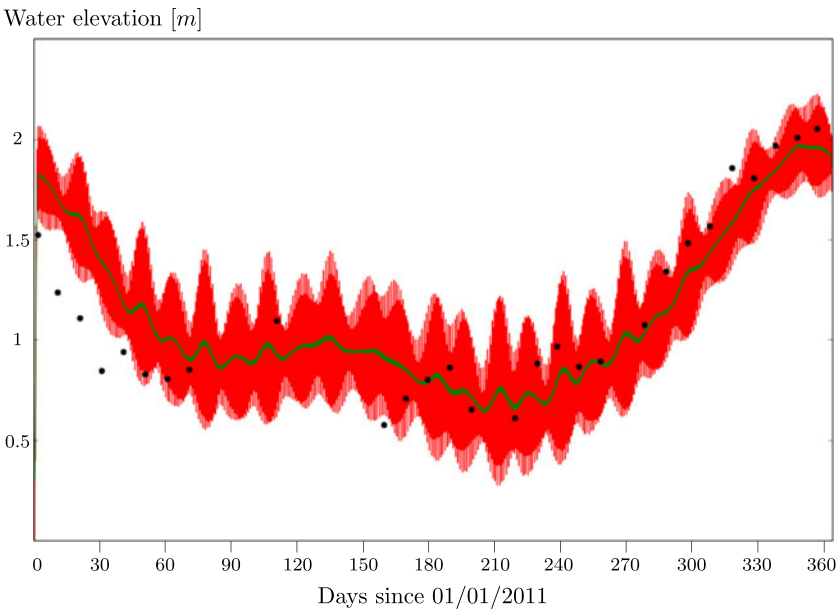

Fig. 7 Water elevation in the Congo River across a 3-km-long river arm between 6.04° S and 6.01° S. Model results for the instantaneous (in *red*) and daily-mean (in *green*) water elevation agree well with observations along the satellite track (•). The river dynamics at that location is influenced both by the tides and the seasonal variations of the river discharge

but is less than half of the signal at the river mouth. The satellite track provides a signal along a 3-km-long segment corresponding to one arm of the river between 6.04° S and 6.01° S. We performed a 1-year simulation over the entire year 2011 and compared the modeled and observed surface elevation along this track. Although this is a more qualitative validation, our results still suggest that the model is able to capture both the river dynamics (driven mostly by the seasonal variability at the inflow) and the tidal signal (see Fig. 7).

4 Analysis of the barotropic hydrodynamics

The validation being satisfactory, our model can now be used to gain some insight into the Congo River hydrodynamics. While the flow is clearly baroclinic in the coastal sea, barotropic effects are dominant in the rest of the domain. The analysis presented here therefore focuses on the system area where the barotropic hypothesis is likely to be relevant.

4.1 River mouth discharge

The rate of discharge at the river mouth (taken here trough a transect at 12.44° E, see Fig. 8) is obviously modulated by the tidal rise and fall of the water surface. However, it is interesting to note that tidal currents are never strong enough to change the direction of the river flow. We have run a 1-year simulation over the year 2011 with the observed river discharge imposed at the upstream boundary in Matadi. At the river mouth, we observe tidal oscillations

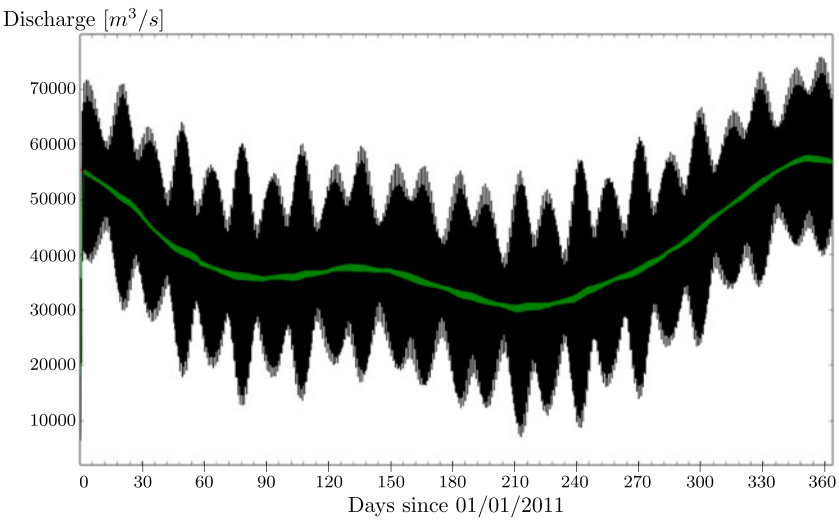

Fig. 8 Congo River discharge simulated at the river mouth taken as a transect located at 12.44° E. The instantaneous discharge (*black curve*) shows the extent of the tidal modulation. When the tidal variations in the time series are filtered out (*green curve*), we recover the discharge imposed at the upstream boundary with a time lag of about 1 day

of about 1.5×10^4 m^3 s^{-1}, which correspond to slightly more than a third of the average discharge. The peak discharge occurs in December with a maximum value of about 7.0×10^4 m^3 s^{-1}. Our simulations suggest that the smallest discharge rates occur in July and August with values of about 1.0×10^4 m^3 s^{-1}. It is noteworthy that this value is quite smaller than the minimal value at the mouth of 2.3×10^4 m^3 s^{-1} estimated by Vanden Bossche and Bernacsek (1990). When the tidal oscillations are removed with a low-pass filter, we recover the discharge imposed at the upstream boundary with a time lag of about one day.

4.2 Instantaneous barotropic currents

In this section, we present simulation results for the month of April 2011 and focus on flow patterns observed in the river section downstream of Boma and in the estuary. Our model suggests that gyres are created in the river mouth as well as in the estuary (see Fig. 9). Such gyres are present both for the instantaneous and residual currents. After the model spin up, they are quite stable in time and space. Even if tides influence the current speed, the gyres appear with similar features at low tide and high tide, as well as during high and low river flow.

To determine what creates these gyres, we have made an extensive sensitivity analysis consisting of several model runs that differ by one element from the setup described in Section 2. Table 3 sums up these runs, and indicates whether gyres were created or not. For every experiment in which the gyres appeared, they always have similar features. In particular, their size is always of about half the width of the estuary, i.e., a few km. The tests suggest the gyres are not a consequence of a lack of resolution, as they are still created with a more refined mesh. Also, they do not appear to be a problem in our implementation of global circulation.

To our knowledge, such gyres have never been mentioned in the literature, nor have they been observed in situ. Such a lack of observation is, however, not surprising since the Congo River remains an understudied system whose dynamics is not well known. It is important to note that these structures do not have the same form as classical numerical instabilities, which are influenced by the mesh size. From the sensitivity analysis that we have conducted, it seems that these instabilities are mostly driven by momentum advection and bottom friction. Such a conjecture is supported by the analysis of the vorticity equation derived from our barotropic model. For the sake of simplicity, let us consider only bottom friction as the only dissipation mechanism and let us neglect all other forcing and dissipation terms in Eq. 2. An equation for the vorticity $\omega = \boldsymbol{e}_z \cdot (\nabla \times \overline{\boldsymbol{u}}) = \frac{\partial v}{\partial x} - \frac{\partial u}{\partial y}$ can then be derived:

$$\frac{\partial \omega}{\partial t} + \nabla \cdot (\overline{\boldsymbol{u}}\omega) + f \nabla \cdot \overline{\boldsymbol{u}} = \boldsymbol{e}_z \cdot \nabla \times \left(-gn^2 \frac{\|\overline{\boldsymbol{u}}\| \overline{\boldsymbol{u}}}{H^{4/3}} \right) \tag{9}$$

$$= -gn^2 \frac{\|\overline{\boldsymbol{u}}\|}{H^{4/3}} \omega - g \left(\nabla \left(\frac{n^2 \|\overline{\boldsymbol{u}}\|}{H^{4/3}} \right) \times \overline{\boldsymbol{u}} \right) \cdot \boldsymbol{e}_z. \tag{10}$$

The last term in Eq. 10 indicates that, in the presence of bottom friction, any variation of the fluid depth or bottom

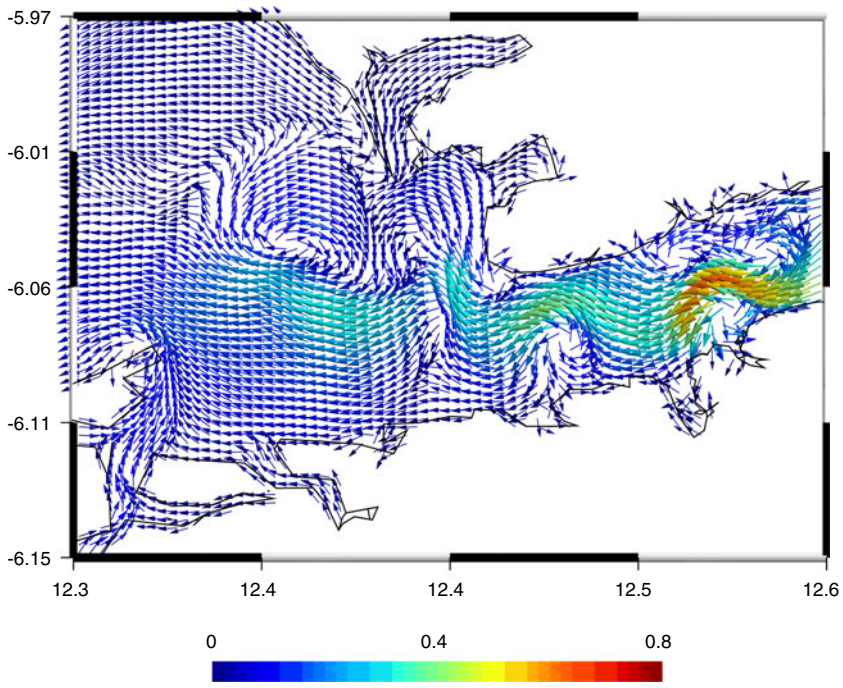

Fig. 9 Instantaneous currents (in ms^{-1}) as simulated for a mean river flow and spring tidal conditions. Gyres are created along the river course and in the adjacent coastal sea

Table 3 Sensitivity analysis scenarios and their consequences on the gyres

Modification with regard to standard model setup	Gyres?	Note
Bathymetry limited to 60 m in river bed (no canyon)	Yes	
No momentum advection	No	
No global circulation	Yes	
No wind forcing	Yes	
No tide	Yes	
No river inflow	Yes	Gravity gradients are the origin of a flow, even when none are given from the boundaries
No river inflow and no river slope forcing	No	Some kind of embryonic gyres do appear just before the shallow area when the tidal flow is strong enough
No gravity gradient	Yes	
No Coriolis' force	Yes	
Strongly diffused bathymetry	Yes	Gyres more downstream in the estuary, mostly because current acceleration spreads more widely in the shallow water area
No navigation channel	Yes	Current even stronger in the shallow water area, gyres appear beyond the river mouth as well
Navigation channel maximum depth set to 50 m	Yes	
Strongly refined mesh in the estuary	Yes	
$n = 5 \times 10^{-2}$ m$^{1/3}$ s	No	
$n = 10^{-2}$ m$^{1/3}$ s	Yes	
$n = 3.5 \times 10^{-2}$ m$^{1/3}$ s	Yes	

roughness that is not locally parallel to the velocity will generate vorticity. Once generated, vorticity immediately becomes subject to advection and frictional decay.

We can now construct a dimensionless number that compares vorticity decay and advection :

$$\kappa = \frac{\text{decay of } \omega}{\text{advection of } \omega} = \frac{gn^2\mathcal{L}}{\mathcal{H}^{4/3}},$$

where $\mathcal{L}$ and $\mathcal{H}$ are a characteristic length and depth of the flow. In the Congo River, gyres seem to appear just downstream of the rather shallow region where the maximum depth is 20 m in the middle of the navigation channel. In the region where gyres are formed, the river depth is of the order of 100 m. It is therefore interesting to compare the value of κ in these two regions. By taking $\mathcal{L} = 10^4$ m, $n = 2.35\times10^{-2}$ m$^{-1/3}$ s and $\mathcal{H} = 10$ m in the shallow region and 100 m in the deeper region, we obtain :

$$\kappa = \frac{9.81\times(2.35\times10^{-2})^2\times10^4}{10^{4/3}} \approx 2.5 \text{ in the shallow region,}$$
$$= \frac{9.81\times(2.35\times10^{-2})^2\times10^4}{100^{4/3}} \approx 0.12 \text{ in the deeper region.}$$

This analysis suggests that friction is strong enough to destroy vorticity in the shallow region. However, in deeper parts of the river, vorticity might not be directly damped and could be advected downstream. Such a conjecture is supported by the work of (Grubišic et al. 1995) who have studied the fate of eddies shed in the wake of an obstacle. They have shown that the steady or unsteady nature of the wake is controlled by a dimensionless bottom friction parameter similar to κ.

Because of the large cloud cover in the region, we were not able to find satellite images that could confirm the presence of these gyres. Instead, we suggest that drifting buoys be deployed to obtain experimental evidence of their existence. To simulate the behavior of such buoys, we have modeled the trajectories of Lagrangian particles. Following Spagnol et al. (2002), we have used the following 2D advection-diffusion equations:

$$\boldsymbol{x}_{n+1} = \boldsymbol{x}_n + \boldsymbol{v}_n\Delta t + \frac{\boldsymbol{R}_n}{\sqrt{r}}\sqrt{2\mu_h\Delta t}, \tag{11}$$

$$\boldsymbol{v}_n = \left(\boldsymbol{u} + \frac{\mu_h}{H}\nabla H + \nabla\mu_h\right)\Big|_{\boldsymbol{x}_n}, \tag{12}$$

where $\boldsymbol{x}_n$ and $\boldsymbol{x}_{n+1}$ are the particle positions at time iterations n and $n+1$, respectively, Δt is the time increment, $\boldsymbol{R}_n$ is a horizontal vector of zero-mean random numbers with variance r, and μ_h is the horizontal diffusivity coefficient. μ_h is determined with Okubo (1971)'s formula: $\mu_h = c\delta^{1.15}$, where $c = 0.03$ m$^{0.85}$ s^{-1} (following de Brye et al. (2012)) and δ is the characteristic size of the element, taken here as square root of the element area.

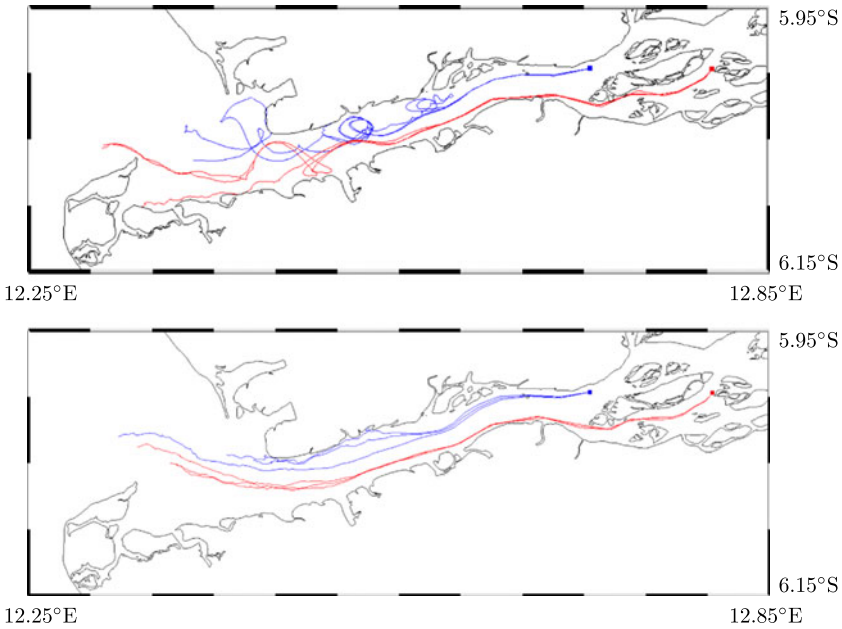

Fig. 10 Trajectories of Lagrangian particles originating from a point located at 6° S, 12.7° E (*blue* trajectories) and another located at 6° S, 12.8° E (*red* trajectories). In both cases, the simulation time is 4 days. In the *top panel*, the momentum-advection terms are not neglected and hence gyres are present. In the *bottom panel*, gyres are absent as momentum advection terms have been neglected. When gyres are present, particles that are transported along the northern river boundary tend to be trapped within the gyres

Figure 10 shows the simulated trajectories of the buoys. Six virtual buoys were released at the same time, three of them at a point located at 6° S, 12.7° E and three others at a point located at 6° S, 12.8° E. The top panel shows the simulated trajectories when gyres are present, while the bottom panel shows the simulated trajectories when gyres are absent because momentum advection has been neglected. When gyres are present, the buoys originating from the first point can be trapped in the gyres, while the other three buoys are transported more quickly toward the river mouth. This indicates that, when gyres are present, particles coming from the northern part of the river are transported by those gyres. These particles may then be trapped for some time close to river boundaries. As the northern part of the river mouth is a mangrove area, this may imply that some constituent carried over by the river would end up in the mangroves. On the contrary, when there are no gyre, trajectories of particles are quite straight. As these trajectories significantly differ, carrying out a similar experiment in the field should help determine whether the gyres actually exist or not.

4.3 Water age

With this hydrodynamic model, we can further analyze the hydrodynamic regimes in the Congo River estuary. To do so, we use the water age as defined in the Constituent-oriented Age and Residence Time theory (CART)[3] (Deleersnijder et al. 2001). Hereafter, water age is defined to be the time elapsed since a particle entered the domain (at $t = t_{in}$). The location of this entry point depends on the phenomena that are investigated. In this study, the age is set to zero at the upstream riverine boundary, i.e., at Matadi. Thus, the water age a is the time elapsed since a water particle enters the domain in Matadi (i.e., $a = t - t_{in}$). It can be modeled with the following transport equation:

$$\frac{\partial}{\partial t}(Ha) + \nabla \cdot (H\overline{\boldsymbol{u}}a) = \nabla \cdot (H\mu_h \nabla a) + H. \tag{13}$$

Equation 13 is a classical transport equation with water depth as source term, representing the ageing rate of the water particles.

We have run a number of 15-days simulations during different period of the year to look at different conditions such as minimum/maximum discharge and neap/spring tides. As can be seen in Fig. 11, our model suggests a particle entering the modeling area at Matadi will reach Boma in less than 24 h. One can see some places where water stagnates, such as the "Chaudron d'enfer" near Matadi, as the water age at such places is significantly greater than in the main channel. Then, after passing Boma, it only takes a couple of days to reach the river mouth when discharge is at its minimum (Fig. 12). The particles are then slowed down by tides entering and leaving the estuary (Fig. 12a), and it takes a few more days to reach Banana. When the river discharge is at its maximum, features are quite the same, but the time to reach Banana is almost 2 days shorter. Figure 12b shows the influence of the gyres described in Section 4.2, as one can see oscillations in the water age structure. The simulation suggests that, depending on the trajectory followed by a given particle, it can enter one or several gyres, and therefore be delayed by few hours.

The sensitivity of the age field to external forcing has been studied by considering maximum/minimum discharge

[3] http://www.climate.be/cart/

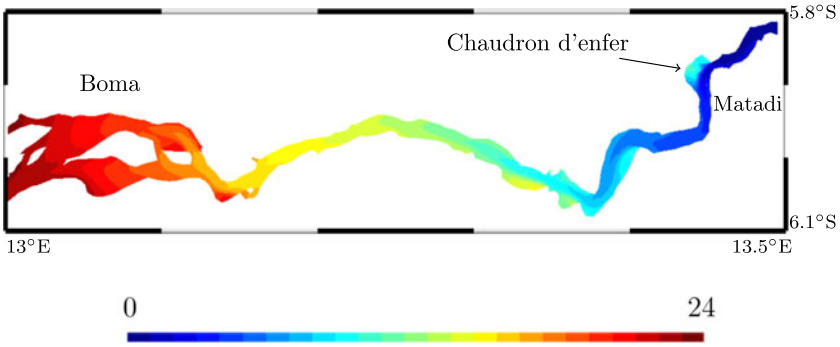

Fig. 11 Water age downstream of Matadi (in h). When entering the domain at Matadi, a particle reaches Boma in about 24 h

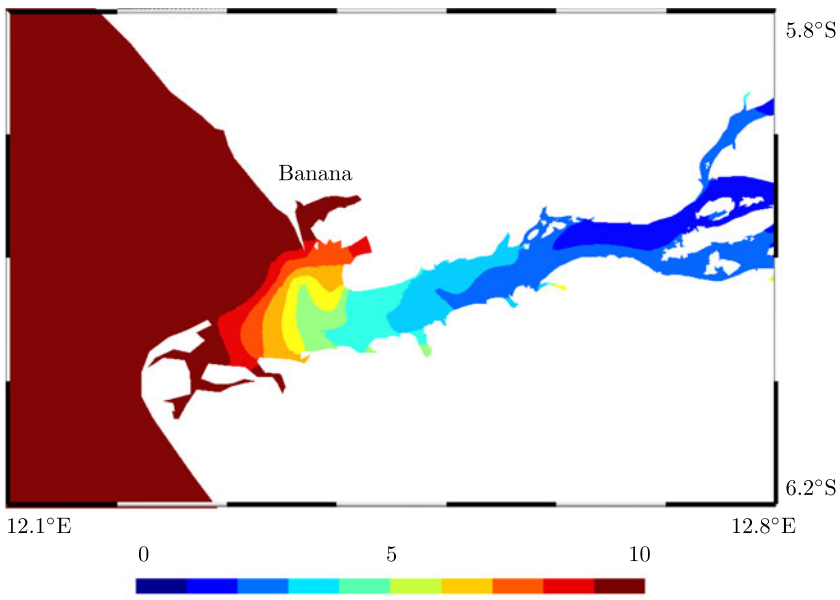

(a) Whole estuary

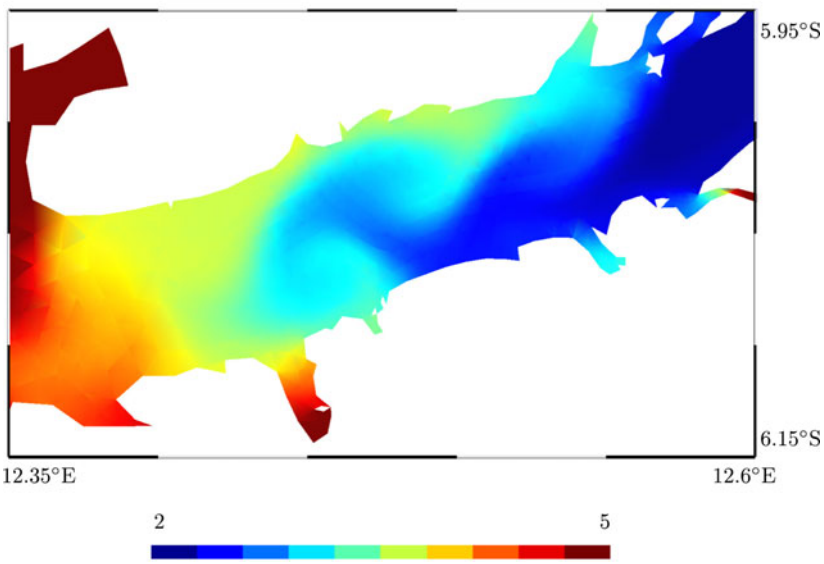

(b) Close-up view on the area where gyres are present

Fig. 12 Water age in Congo River mouth (in days) when river discharge is at its minimum. Entering the domain in Matadi, a particle reaches the river mouth in 2 days. It takes several more days for the particle to actually reach the deep ocean

and spring/neap tide scenario. A particle leaving Matadi will reach Banana in 9 days when the river discharge is at its minimum. When the discharge is at its maximum, a particle seeded from Matadi reaches Banana in 6 days. Similar features are observed for the tidal regime. When tides are at their maximum, the water age at a given point in the river mouth can be several hours greater than the water age at the same point when tides are at their minimum. In our barotropic modelling, wind stress and global circulation have a negligible impact on the water age. However, such phenomena usually influence stratification. Therefore, we can expect that baroclinic modelling will show that these phenomena have more impact, especially on the plume dynamics.

5 Conclusion

In this study, we have used a multi-scale, unstructured-mesh model to simulate the hydrodynamics of the Congo River continuum from the downstream end of the rapids in Matadi to the deep ocean. While this study only considers barotropic processes and is still only the first step of a larger effort, it nonetheless describes the first simulations of the entire Congo river-estuary-coastal sea continuum. Such a study would have been impossible with a more traditional structured-mesh model as it would have required to nest several model within each others to downscale from regional to local scales. Instead, using an unstructured mesh allows for an integrated approach, where the coastal model is the same as the river model and the mesh spatial resolution is finely adapted to the characteristic scale of the phenomena under study. Another step further in establishing an integrated approach has been to combine hydrologic modeling (to take the riverbed slope into account) with coastal ocean modelling approaches.

Obviously, using a depth-averaged model has its limitations. While in the river and the shallower parts of the estuary and coastal zone, our model appears capable of reproducing the dominant features of the hydrodynamics. This statement is probably much less relevant in the region of the canyon. It is hard to imagine what would be the key modifications to the hydrodynamics as this canyon is specific to the Congo River and has no counterpart elsewhere to the best of our knowledge. We can only underscore that the model reproduces the tidal signal quite well, suggesting that the impact of the density variations on the barotropic mode may not be dominant in the domain of interest.

After having validated our model in the sea and river environment, we have used it to examine instantaneous currents. Gyres are created along the river and in the neighbouring coastal sea. The vorticity budget suggests that these gyres could be controlled by the interplay between momentum advection and bottom friction. To investigate barotropic dynamics time scale in this area, we have used age theory. In this case, our 2D model shows that the most intense hydrodynamic phenomenon is the river discharge. Tidal dynamics come just after, and can even compete with river discharge in the river mouth when tide currents are the most intense. Considering only barotropic phenomena, global circulation and wind are not as important.

Acknowledgments The financial support of Total EP Recherche Développement and CLS (under contract CLS-DOS-13-003) is gratefully acknowledged. SLIM is developed under the auspices of the Action de Recherche Concertée “Taking up the challenges of multi-scale marine modelling” funded by the Communauté française de Belgique under contract ARC 10/15-028. Some of the computational resources were provided by the Consortium des Équipements de Calcul Intensif (CÉCI), funded by the F.R.S.-FNRS under Grant No. 2.5020.11. Yoann Le Bars is indebted to Christopher Thomas for his comments and constructive criticism during the preparation of the present manuscript. Éric Deleersnijder is an honorary Research associate with the F.R.S.-FNRS.

Appendix A: Data collection and treatment

In this section, we briefly describe the procedures we had to develop in order to extract and merge different sources of information in order to construct the bathymetry and coastline datasets. Although quite technical, this preliminary step was absolutely necessary due to the scarcity of data readily available for that region.

A.1 Bathymetry

Several global bathymetric datasets are available. As a basis for our digital bathymetry, we used GEBCO 2008 (Monahan 2008). This bathymetry dataset provides a 30″ regular grid of sounding points. This is sufficient in basin areas but not close to the coasts and inside the river. To complement GEBCO 2008, we have therefore collected nautical charts. These charts were edited in 2003 and 2008 but cover only the Congo River estuary. The shallow water part of the river that spreads about 35 km downstream of Boma is very poorly charted. There are no certified bathymetry dataset for this region. This is obviously problematic since water depth strongly influences bottom friction, which plays an important role in shallow regions. In this area, a channel for commercial navigation is maintained. The maximum allowed draught is known along this channel, but neither its actual depth nor its width.

To collect data from paper charts, we have developed a piece of software, GeoDesk[4], which is freely available. First, charts need to be digitalized, using wide size scanners.

[4] http://ylebars.github.io/GeoDesk/

Then, GeoDesk can georeference the resulting images and collect data such as bathymetric sounding and isobathymetric lines.

GEBCO 2008 reference is the mean water level, while in nautical charts we have used it is minimum water level. In our model, the reference is the mean water level, which is a standard choice. To make data from nautical charts fit this reference, we have added half the tidal range on them, which we have obtained from our model. This correction has been done until convergence, i.e., until no impact is noticeable on the tidal modeling. In the case of our Congo River model, only one iteration was necessary.

In the unobserved area, we have assumed the depth to be 5 m. The navigational channel is assumed to be 20 m deep at its maximum and 1 km wide, with a parabolic depth profile. These choices are consistent with the little information available.

All of these developments lead to the bathymetry displayed in Fig. 3. This digital bathymetry uses an unstructured approach: the resolution is a function of how many sounding points we had. Hence, in the areas where nautical charts are well defined, the resolution is of the order of 10 m. In the deep ocean, the resolution is the same as the one of GEBCO 2008. The bathymetry is then interpolated on the unstructured mesh of the hydrodynamic model (described in Section 2).

A.2 Coastlines

As a starting point, we have used the Global Self-consistent, Hierarchical, High-resolution Geography (GSHHG) database (Wessel and Smith 1996), which is a digital database of global coastlines. At the river mouth, we have completed this coastline using the previously digitalized charts. These images have been vectorized using Gimp[5] and Inkscape[6]. We have then obtained a vectorial image in SVG format, and we used GeoDesk to georeference it. A locally-developed tool finally converts the image into a format our model can use.

References

Burke K (1972) Longshore drift, submarine canyons and submarine fans in development of Niger delta. Bull Am Assoc Pet Geol 56(10):1975–1983

Carrère L, Lyard F, Cancet M, Guillot A, Roblou L (2012) FES2012: A New Global Tidal model taking advantage of nearly 20 years of altimetry In: Proceedings of Meeting "20 years of altimetry". Esa publication, Venice

Chassignet EP, Hurlburt HE, Smedstad OM, Halliwell GR, Hogan PJ, Wallcraft AJ, Baraille R, Bleck R (2007) The HYCOM (HYbrid Coordinate Ocean Model) data assimilative system. J Mar Syst 65(1–4):60–83. doi:10.1016/j.jmarsys.2005.09.016

de Brye B, de Brauwere A, Gourgue O, Karna T, Lambrechts J, Comblen R, Deleersnijder E (2010) A finite-element, multi-scale model of the Scheldt tributaries, river, estuary and ROFI. Coast Eng 57(9):850–863. doi:10.1016/j.coastaleng.2010.04.001

de Brye B, Schellen S, Sassi M, Vermeulen B, Karna T, Deleersnijder E (2011) Preliminary results of a finite-element, multi-scale model of the Mahakam Delta (Indonesia). Ocean Dyn 61:1107–1120. doi:10.1007/s10236-011-0410-y

de Brye B, de Brauwere A, Gourgue O, Delhez E, Deleersnijder E (2012) Water renewal timescales in the Scheldt Estuary. J Mar Syst 94:74–86

Deleersnijder E, Campin J, Delhez EJM (2001) The concept of age in marine modelling: I. Theory and preliminary model results. J Mar Syst 28(3–4):229–267

Denamiel C, Budgell WP, Toumi R (2013) The Congo River plume: impact of the forcing on the far-field and near-field dynamics. J Geophys Res Oceans 118:964–989. doi:10.1002/jgrc.20062

Eisma D, Kalf J (1984) Dispersal of Zaire river suspended matter in the estuary and Angola basin. Neatherlands Journal of Sea Research 17(2–4):385–411

Eisma D, van Bennekom AJ (1978) The Zaire River and estuary and the Zaire outflow in the Atlantic Ocean. Neth J Sea Res 12(3/4):255–272

Eisma D, Kalf J, van der Gaast SJ (1978) Suspended matter in the Zaire estuary and the adjacent Atlantic. Neatherlands Journal of Sea Research 12(3/4):382–406

Flather RA (1976) A tidal model of the north-west European continental shelf. Mémoires de la Société royale des sciences de Liège 6(10):141–164

Geuzaine C, Remacle JF (2009) GMSH A three-dimensional finite element mesh generator with built-in pre- and post-processing facilities. Int J Numer Methods Eng 79(11):1309–1331. doi:10.1002/nme.2579

Graf WH, Altinakar MS (1993) Hydraulique fluviale, tome 1 : Écoulement permanent uniforme et non uniforme, Traité de génie civil de l'École polytechnique fédérale de Lausanne, vol 16, 1st edn. Presses polytechniques et universitaires romandes, CH-1015 Lausanne

Graf WH, Altinakar MS (1996) Hydraulique fluviale, tome 2 : Écoulement non permanent et phénomènes de transport, Traité de génie civil de l'École polytechnique fédérale de Lausanne, vol 16, 1st edn. Presses polytechniques et universitaires romandes, CH-1015 Lausanne

Grubišic V, Smith RB, Schär C (1995) The effect of bottom friction on shallow-water flow past an isolated obstacle. J Atmos Sci 52(11):1985–2005

Heezen BC, Menzies RJ, Schneider ED, Ewing WM, Granelli NCC (1964) Congo submarine canyon. Bull Am Assoc Pet Geol 48(7):1126–1149

Hervouet J-M, Van Haren L (1996) Recent advances in numerical methods for fluid flow. In: Anderson M, Walling D, Bates P (eds) Floodplain processes. Wiley, Chichester, p 183

Hopkins J, Lucas M, Dufau C, Sutton M, Stum J, Lauret O, Channelliere C (2013) Detection and variability of the Congo River plume from satellite derived sea surface temperature, salinity, ocean colour and sea level. Remote Sens Environ 139:365–385. doi:10.1016/j.rse.2013.08.015

Jansen PP (1979) Principles of River Engineering: The Non-tidal Alluvial River. Addison-Wesley Educational Publishers Inc

Lambrechts J, Comblen R, Legat V, Geuzaine C, Remacle JF (2008a) Multiscale mesh generation on the sphere. Ocean Dyn 58(5):461–473. doi:10.1007/s10236-008-0148-3

[5] http://www.gimp.org/

[6] http://www.inkscape.org/

Lambrechts J, Hanert E, Deleersnijder E, Bernard PE, Legat V, Remacle JF, Wolanski E (2008b) A multi-scale model of the hydrodynamics of the whole Great Barrier Reef. Estuar Coast Shelf Sci 79(1):143–151. doi:10.1016/j.ecss.2008.03.016

Lyard F, Lefèvre F, Letellier T, Francis O (2006) Modelling the global ocean tides: modern insights from FES2004. Ocean Dyn 56:394–415

Martinsen EA, Engedahl H (1987) Implementation and testing of a lateral boundary scheme as an open boundary condition in a barotropic ocean model. Coast Eng 11:603–627

Meulenbergh J (1968) Diffusion des eaux du fleuve Congo dans les eaux de l'Atlantique sud. Acad Roy Sc d'outre-mer. Cl Sci Tech (NS) 16(6):1–149

Meulenbergh J (1974) La mangrove zaïroise. Acad Roy Sc d'outre-mer. Cl Sci Tech (NS) 17(8):1–86

Monahan D (2008) Mapping the floor of the entire world ocean: the general bathymetric chart of the oceans. Journal of Ocean Technology 3(1):108

Okubo A (1971) Oceanic diffusion diagrams. Deep-sea Res 18:789–802

Peters JJ, Sterling A (1973) Étude de l'amélioration du bief maritime du fleuve Zaïre. Laboratoire de recherches hydrauliques, Borgerhout, Anvers Mateba 10:1–19

Savoye B, Babonneau N, Dennielou B, Bez M (2009) Geological overview of the Angola-congo margin, the Congo deep-sea fan and its submarine valleys. Deep-Sea Res II 56:2169–2182. doi:10.1016/j.dsr2.2009.04.001

Smith SD, Banke EG (1975) Variation of the sea surface drag coefficient with wind speed. Q J R Meteorol Soc 101:665–673

Spagnol S, Wolanski E, Deleersnijder E, Brinkman R, McAllister F, Cushman-Roisin B, Hanert E (2002) An error frequently made in the evaluation of advective transport in two-dimensional lagrangian models of advection-diffusion in coral reef waters. Mar Ecol Prog Ser 235:299–302

Thomas CJ, Lambrechts J, Wolanski E, Traag VA, Blondel VD, Deleersnijder E, Hanert E (2014) Numerical modelling and graph theory tools to study ecological connectivity in the Great Barrier Reef. Ecol Model 272(0):160–174. doi:10.1016/j.ecolmodel.2013.10.002

Vanden Bossche JP, Bernacsek GM (1990) Source Book for the Inland Fishery Resources of Africa. No. vol. 1 in CIFA technical paper, Food and Agriculture Organization of the United Nations

Wessel P, Smith WHF (1996) A Global Self-consistent, Hierarchical, High-resolution Shoreline Database. J Geophys Res 101(B4):8741–8743